# Modeling the User's Body Effects on a 5G Millimeter-Wave Cellphone Antenna Array

Bing Xue, *Graduate Student Member, IEEE*, Katsuyuki Haneda, *Member, IEEE*, Pasi Koivumäki, *Member, IEEE*, and Clemens Icheln

***Abstract*— 5G millimeter-wave (mmW) wireless communication is an important study hotspot in recent years. The human blockage has been a part of multipath radio channels, and its extra losses to received powers of wireless links are modeled in different works. This manuscript aims at establishing an analytically tractable and hence fast way to estimate user body effects on radiations of cellphone antennas at mmW frequencies. Mathematical operators are first defined to represent the user body effects on cellphone antenna radiation where shadowing and backscattering are modeled through knife-edge diffraction (KED) and geometrical optics (GO). Next, the proposed operators are tested for a cellphone antenna array that is held in landscape and portrait modes. Agreement of radiation pattern cuts and spherical coverage statistics is observed between full-wave simulations with complex human body models and our proposed mathematical operators. Finally, compared with full-wave simulations, the proposed model has a clear computational advantage in predicting user body effects on cellphone radiations without the need for a complex human body model, while maintaining a decent level of accuracy. The proposed operators, therefore, contribute to expediting the calculation of antenna–body interaction in mmW cellphone communication channel simulations.**

***Index Terms*— Cellphone antenna array, channel simulations, mathematical model, millimeter-wave (mmW), user-effect modeling.**

## I. Introduction

MILLIMETER-WAVE (mmW) wireless communication has been a significant research highlight in recent years. When studying radio links of mmW bands, ensuring robust connectivity in dynamic electromagnetic scenarios is a key issue. Human blockage is an influential part of the wireless communication environment that affects mmW connectivity. There are studies on this issue, including loss models [1], [2], [3], [4], [5], [6], [7], [8], [9], [10], [11], [12] and relevant measurements [4], [5], [10], [13], [14], [15], [16]. In these studies, the human blockage is a part of the radio *environment* and hence *multipath propagation channel*, where theories of diffraction are used to model the additional losses to the received power. When a human is the user of a cellphone, researchers generally consider their effects as a part of *antennas*. The effects have been evaluated in [17], [18], [19], [20], [21], [22], [23], [24], and [25] because they are also essential for link connectivity studies. However, the evaluations are through measurements of a cellphone prototype or electromagnetic simulations including the full human body, which are laborious and time-consuming due to the electrically large human body at mmW frequencies. A faster way to predict the radiation patterns of a cellphone antenna array in the presence of a user would, therefore, be useful. This article develops *an analytical model* to evaluate the body effects of a cellphone user on cellphone antenna radiation. The model is formulated as mathematical operators applied to radiation patterns of a cellphone antenna array, held in users' hands, such that radiation patterns of a cellphone antenna array with the presence of the entire body of a user are obtained. Required inputs to the operator are the dimensions of a referential human body along with the phone orientation, with which the shadowing and backscattering effects on the radiation of a cellphone array due to the user body are calculated. No complex body model, let alone dimension measurements of a body are required in defining the operator, allows us to predict the user body effects more accurately than the present state-of-the-art in [26] where the self-blockage model in Section 7.6.4.1 adopts binary attenuation levels. The efficacy of the operator has been verified against full-wave simulations using a complex user body model, which were verified against measurements in our previous article [19], [21]. The innovations reported in this article are summarized as follows.

1) Showing that the absorbing knife-edge diffraction (KED), which is traditionally used to model the user's body effects on the Fraunhofer region of wave propagation, can be used to predict the *shadowed region* of the radiation patterns of the cellphone antenna due to a user body in the Fresnel region.
2) Applying the geometrical optics (GO) to a simple human body structural model, consisting of cylinder and spheres, to model user backscattering effects on the *lit region* of the radiation patterns of the cellphone antenna.

Manuscript received 6 May 2023; revised 18 December 2023; accepted 5 January 2024. Date of publication 22 January 2024; date of current version 7 March 2024. This work was supported in part by the Academy of Finland–NSF joint call pilot "Artificial Intelligence and Wireless Communication Technologies," decision under Grant 345178. *(Corresponding author: Bing Xue.)*

The authors are with the Department of Electronics and Nanoengineering, School of Electrical Engineering, Aalto University, FI-00076 Espoo, Finland (e-mail: bing.xue@aalto.fi).

Color versions of one or more figures in this article are available at https://doi.org/10.1109/TAP.2024.3353931.

Digital Object Identifier 10.1109/TAP.2024.3353931

3) Verifying correctness of the mathematical operators to describe shadowing and backscattering of radiated fields from a cellphone antenna array; the fields with the user's body effects are compared to the ground truth of complex full-wave simulations, showing that the realistic user's body effects can be considered in radio link and system simulations with much less computational efforts than full-wave simulations.

It must be noted that the mathematical operator does not cover the influence of cellphone user's hands on the radiation of cellphone antennas. Different from body effects, hands modify current distributions and near-fields of antennas, which are too complex phenomena to model analytically. The operator, therefore, needs radiation patterns of a cellphone with the influence of the user's hands as inputs, or it needs radiation patterns of a cellphone in free space when there is no hand effect.

The rest of the article is arranged as follows. Section II introduces the principles of modeling the user's body effects on radiation patterns and then shows the mathematical operators to model user body effects. The evaluation metric, that is, spherical coverage, is introduced. After introducing the user hand models to define inputs to the operator, Section III compares radiated fields calculated with the referential complex numerical human model and with the proposed operator. The time costs of the calculation are given. Finally, conclusions are summarized in Section IV, followed by the Appendix illustrating some essential mathematical formulas to understand the proposed mathematical operator.

## II. Modeling Body Effects on Antenna Radiation Patterns

In this section, we bring in an operator to represent user body effects on radiations of cellphone antennas. Then, a metric to compare body-influenced radiation patterns is illustrated.

### A. Definition of the Operator Representing the User Body Effects

Radiation patterns of a cellphone antenna with the user's whole body effect are related to those with only hand effects by

$$G_{\text{body}}(\boldsymbol{\Omega}, f) = F_{\text{body}}(\boldsymbol{\Omega}, f) G_0(\boldsymbol{\Omega}, f) \tag{1}$$

where $F_{\text{body}}(\boldsymbol{\Omega}, f)$ is an operating function representing user body effects at a spatial angle $\boldsymbol{\Omega} = [\theta, \phi]$ over a sphere[1] and at a frequency $f$; $G_{\text{body}}(\boldsymbol{\Omega}, f)$ indicates an antenna's realized gain with the user's whole body effects and $G_0(\boldsymbol{\Omega}, f)$ indicates an antenna's realized gain with the user's hand effects. For brevity, we omit $f$ in the following since we discuss antenna gains at a specific frequency $f_0$. This work aims to derive $F_{\text{body}}(\boldsymbol{\Omega})$ analytically.

[1]In this article, the spherical-coordinate variable $\theta$ starts from the positive direction of the $z$-axis; the spherical-coordinate variable $\phi$ starts from the positive direction of the $x$-axis.

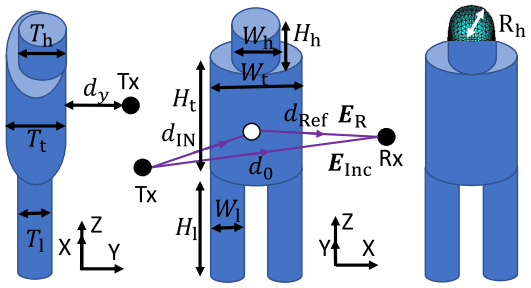


Fig. 1. Schematic of the proposed reflection model for the lit region; the white point shows a reflection point; the green structure represents the upper hemisphere of the human head for modeling the region above the head top.

### B. From Full-Wave Simulations to Analytical Calculations

When using full-wave simulations to solve the user's head and torso effects on cellphone antenna radiation, cylinder-like structures have been popularly used to represent user [19], [20]. They showed an excellent agreement of radiated fields with empirical statistics at 5G mmW frequencies. Following them, we use cylinders and spheres to represent the human body. At mmW frequencies, it is sufficient to study skin effects instead of including internal structures of a human [19], [27] since the skin depth of electromagnetic fields is shallower than 2 mm for human skin. Most human bodies are electrically large in size at mmW bands and hence, transmissions of fields through the body and diffractions brought from creeping waves can be ignored [28]. Only edge diffractions, reflections, and transmissions in free space are, therefore, included in the proposed model instead of full-wave simulations to derive radiated fields with user body effects. Based on GO, radiation patterns with body effects are divided into two major regions, that is, the shadowed region and the lit region, where diffraction beyond the body and backscattering on the body are prevalent, respectively [29]. Additionally, a near-shadowed region must be defined as a transition between the two where it is a lit region, but diffracted fields cannot be neglected.

### C. Lit Region

For the lit region, scattering of electrically large objects can be estimated by reflections and diffractions [29]. Since the human is electrically large in size at mmW, diffracted fields from body edges are much weaker than reflected fields in the lit region, especially where the backscattering is prevalent. When analyzing wave reflection, incident electromagnetic waves on a medium interface usually assume far fields of a plane wave source. In contrast, in our case, the incident waves on the human body are like spherical waves since the antenna source is in the user's hands. Therefore, curvature-based GO with a spherical source is applied. In our analytical model to estimate the backscattered fields, a user body is simplified by a combination of several elliptical cylinders shown in Fig. 1. Apart from these cylinders, a semisphere is used to model the region above the head top. The arms are a part of the torso. The body's dimensions are summarized in Table I, which are identical to the later calculation of fields in the shadowed region. In addition, depths are defined for the cylindrical head, torso, and legs as illustrated in Fig. 1.

TABLE I
DIMENSIONS OF THE HUMAN MODEL

| | Shadow | Lit | values [cm] |
|---|---|---|---|
| Head width ($W_{\rm h}$) | ✓ | ✓ | 14.8 |
| Head height ($H_{\rm h}$) | ✓ | ✓ | 26.0 |
| Head Thickness ($T_{\rm h}$) | | ✓ | 14.8 |
| Torso width ($W_{\rm t}$) | ✓ | ✓ | 52.0 |
| Torso height ($H_{\rm t}$) | ✓ | ✓ | 80.0 |
| Torso Thickness ($T_{\rm t}$) | | ✓ | 25.0 |
| Leg width ($W_{\rm l}$) | ✓ | ✓ | 15.0 |
| Leg height ($H_{\rm l}$) | ✓ | ✓ | 69.0 |
| Leg Thickness ($T_{\rm l}$) | | ✓ | 15.0 |
| Semi-sphere radius($R_{\rm h}$) | | ✓ | 7.4 |

Given the mobile antenna location and far-field angle $\boldsymbol{\Omega}_{\rm lit}$, the Fermat principle determines reflection points on the body [30]. Let us define $\boldsymbol{E}(\boldsymbol{\Omega}) = [E_\theta(\boldsymbol{\Omega})\ E_\phi(\boldsymbol{\Omega})]^{\mathsf{T}}$ to be a polarimetric electric field vector in the spherical coordinate system where $\cdot^{\mathsf{T}}$ is the transpose operator. When knowing the locations of the radiating antenna source and a field observation point, we can define an operator $\tilde{F}_{\rm body}(\boldsymbol{\Omega}_{\rm lit}, d_0)$ by

$$\tilde{F}_{\rm body}(\boldsymbol{\Omega}_{\rm lit}, d_0) = \frac{\|\boldsymbol{E}_{\rm R}(\boldsymbol{\Omega}_{\rm lit}, d_0) + \boldsymbol{E}_{\rm Inc}(\boldsymbol{\Omega}_{\rm lit}, d_0)\|_2^2}{\|\boldsymbol{E}_{\rm Inc}(\boldsymbol{\Omega}_{\rm lit}, d_0)\|_2^2} \tag{2}$$

where $d_0$ is the distance between the source and field observation points, $\|\cdot\|_2$ is the 2-norm operator, $\boldsymbol{\Omega}_{\rm lit}$ is the solid angle corresponding to the lit region of the mobile antenna source, and $\boldsymbol{E}_{\rm R}(\boldsymbol{\Omega}_{\rm lit}, d_0)$ is the reflected complex electric far-field defined by

$$\boldsymbol{E}_{\rm R}(\boldsymbol{\Omega}_{\rm lit}, d_0) = T_{\rm c}(d_{\rm Ref})\boldsymbol{C}_{\rm gl}\boldsymbol{R}_{\rm l}\boldsymbol{C}_{\rm lg}\boldsymbol{E}_{\rm Inc}(\boldsymbol{\Omega}_{\rm inc}, d_{\rm IN}) \tag{3}$$

where the incident angle and distance of the reflected field on the body, $\boldsymbol{\Omega}_{\rm inc}$ and $d_{\rm IN}$, respectively, define the reflection-point coordinates; $d_{\rm Ref}$ is the distance between the reflection point and the field observation point; $\boldsymbol{C}_{\rm lg}$ and $\boldsymbol{C}_{\rm gl} \in \mathbb{R}^{2\times 2}$ define field conversion matrices between the global spherical coordinate system and the local curvature coordinate system on the body where the reflection point is located [29], [31], respectively; $\boldsymbol{R}_{\rm l} \in \mathbb{C}^{2\times 2}$ is the reflection coefficient matrix defined by

$$\boldsymbol{R}_{\rm l} = \begin{bmatrix} \Gamma_{\rm p} & 0 \\ 0 & \Gamma_{\rm v} \end{bmatrix} \tag{4}$$

where $\Gamma_{\rm p}$ and $\Gamma_{\rm v}$ are, respectively, for the parallel and perpendicular polarizations on body surfaces [32], Chapter 1.8. Any incident fields at an observation location $\boldsymbol{E}_{\rm Inc}(\boldsymbol{\Omega}, d)$ can be written as

$$\boldsymbol{E}_{\rm Inc}(\boldsymbol{\Omega}, d) = \frac{\lambda_0 \boldsymbol{E}_0(\boldsymbol{\Omega})}{4\pi d} \exp\left(-{\rm j}2\pi \frac{d}{\lambda_0}\right) \tag{5}$$

where ${\rm j} = \sqrt{-1}$, $\lambda_0$ is the operating wavelength in free space; $\boldsymbol{E}_0(\boldsymbol{\Omega})$ represents far-field complex magnitude at a source, and $d$ is the distance between the source and observation locations. Now $T_{\rm c}(d_{\rm Ref})$ in (3) can be written as

$$T_{\rm c}(d_{\rm Ref}) = \sqrt{\frac{\rho_{\rm r,1}\rho_{\rm r,2}}{(\rho_{\rm r,1}+d_{\rm Ref})(\rho_{\rm r,2}+d_{\rm Ref})}} \exp\left(-{\rm j}2\pi \frac{d_{\rm Ref}}{\lambda_0}\right) \tag{6}$$

where $\rho_{\rm r,1}$ and $\rho_{\rm r,2}$ are the principal radii of body curvature at the reflection point, respectively, which are defined in the Appendix. In (3), possible multiple reflections between the user's hands, arms, and torso are neglected to simplify our model since: 1) multiple-bounce rays are produced by hands, the cellphone, and forearms that are smaller than the torso, making their power contribution not as significant as those single-bounce rays from the torso; and 2) every reflection leads to a larger than 3-dB loss at mmW frequencies [33]. Hence, our model only includes the line-of-sight (LOS) and the single-bounce reflected signals.

To derive $\hat{F}_{\rm body}(\boldsymbol{\Omega}_{\rm lit})$ which aims at representing the measured and simulated observations of $F$ defined in Section II-A, we can assume that the field observation point is far enough from the body, that is, $d_0 \to \infty$, leading to $d_{\rm Ref} \approx d_0 \gg \rho_{\rm r,1}$ and $\rho_{\rm r,2}$. Now (2) yields

$$\begin{aligned}\hat{F}_{\rm body}(\boldsymbol{\Omega}_{\rm lit}) &= \lim_{d_0\to\infty} \tilde{F}_{\rm body}(\boldsymbol{\Omega}_{\rm lit}, d_0) \\ &= \frac{\left\|K_{\rm t}\boldsymbol{C}_{\rm gl}\boldsymbol{R}_{\rm l}\boldsymbol{C}_{\rm lg}\boldsymbol{E}_0(\boldsymbol{\Omega}_{\rm inc}) + \boldsymbol{E}_0(\boldsymbol{\Omega}_{\rm lit})\right\|_2^2}{\|\boldsymbol{E}_0(\boldsymbol{\Omega}_{\rm lit})\|_2^2}\end{aligned} \tag{7}$$

where $K_{\rm t} = ((\rho_{\rm r,1}\rho_{\rm r,2})^{1/2}/d_{\rm IN})\exp(-{\rm j}2\pi(d_\Delta/\lambda_0))$, and $d_\Delta = d_{\rm IN} + \boldsymbol{d}_{\rm IN}\cdot\boldsymbol{s}$ is the extra propagation distance of the reflection path compared with the LOS path; $\boldsymbol{s}$ is the unit vector of the angle $\boldsymbol{\Omega}_{\rm lit}$.

### D. Shadowed Region

*1) Existing Human Blockage Models in the Fraunhofer Region of Antennas:* When establishing mathematical models to discuss the body effects for the shadowed region, a cylinder or an elliptical cylinder is used [1], [3] to model a human. They work in 2-D cases but not always for 3-D scenarios. Some others used a model based on conducting and insulating screens and wedges [4], [6], [34]. The other papers mainly adopted KED models to describe the shadowed region where a human body is considered as an absorbing screen, for example, [9]. It is worth noticing that the formulas of KED assume infinitely long edges/wedges. However, it still is a good approximation also for short edges [2], [5], [9], [13], [29], [35] representing, for example, the right and the left of the torso, leading to multiple-KED models. These KED models evaluate human blockage effects in a plane-wave multipath channel, which are usually defined as far fields of antennas. However, in our case, mobile antennas are in the user's hands, and, moreover, they illuminate the human body through spherical waves. We examine whether the KED models, defined in the Fraunhofer region, apply to the Fresnel region of radiated fields from mobile antennas in typical use cases of portrait and landscape hand grip modes.

*2) Proposed Body Effect Model in the Fresnel Region of Antennas:* A user body is modeled as a combined absorbing screen shown in Fig. 2. The rear arms are a part of the torso. The parameter values of the absorbing screen are summarized in Table I, which are identical to those of the body model used for the lit region in Section II-C. For simplicity, thighs are modeled as a part of the torso and calves are modeled as separate legs. Then, similar to the lit region, the mathematical operator $\tilde{F}_{\rm body}(\boldsymbol{\Omega}_{\rm shadow}, d_0)$ is represented by

$$\tilde{F}_{\rm body}(\boldsymbol{\Omega}_{\rm shadow}, d_0) = \frac{\|\boldsymbol{E}_{\rm T}(\boldsymbol{\Omega}_{\rm shadow}, d_0)\|_2^2}{\|\boldsymbol{E}_{\rm Inc}(\boldsymbol{\Omega}_{\rm shadow}, d_0)\|_2^2} \tag{8}$$

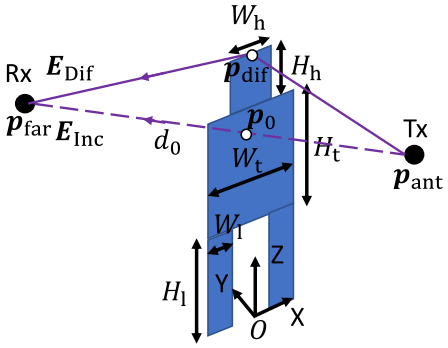


Fig. 2. Schematic of the proposed knife-edge model of a human body for the shadowed region; coordinate origin: $\boldsymbol{O} = (0, 0, 0)$.

where $\boldsymbol{\Omega}_{\text{shadow}}$ is the spatial angle of antennas' radiation patterns in the user-shadowing region; $\boldsymbol{E}_{\text{Inc}}(\boldsymbol{\Omega}_{\text{shadow}})$ is given in (5); $\boldsymbol{E}_{\text{T}}(\boldsymbol{\Omega}_{\text{shadow}}, d_0)$ can be obtained by the sum of diffraction fields due to $N$ knife edges, written as

$$\boldsymbol{E}_{\text{T}}(\boldsymbol{\Omega}_{\text{shadow}}, d_0) = \sum_{i=1}^{N} \boldsymbol{E}_{\text{Dif},i}(\boldsymbol{\Omega}_{\text{shadow}}, d_0) \exp\left(-\text{j}2\pi \frac{\Delta d_i}{\lambda_0}\right) \tag{9}$$

where $\Delta d_i$ is the extra propagation distance of the $i$th diffraction path compared with the LOS path; $\boldsymbol{E}_{\text{Dif},i}(\boldsymbol{\Omega}_{\text{shadow}}, d_0) = C_{\text{Dif},i}\boldsymbol{E}_{\text{Inc}}(\boldsymbol{\Omega}_{\text{shadow}}, d_0)$ is a diffracted field, where $C_{\text{Dif},i} = ((1+\text{j})/2)[((1/2) - C(v_i)) - \text{j}((1/2) - S(v_i))]$; $C(v)$ and $S(v)$ correspond with cosine and sine Fresnel integrals represented by, for example, the formula (4) in Appendix A of [9]. It must be noted that KED provides a polarization-independent diffraction coefficient. Let us denote $\boldsymbol{p}_0 = [p_x, p_y, p_z]$ a coordinate on the body where a ray path launched from the mobile antenna location $\boldsymbol{p}_{\text{ant}}$ to a user-shadowing angle $\boldsymbol{\Omega}_{\text{shadow}}$ hits, as defined in Fig. 2; $\boldsymbol{p}_{\text{far}}$ is the field observation location. Another coordinate on a knife edge $\boldsymbol{p}_{\text{dif}}$ represents a diffracted point of a path on the body. Then, we can obtain

$$\Delta d = \left\|\boldsymbol{p}_{\text{dif}} - \boldsymbol{p}_{\text{ant}}\right\|_2 - \left\|\boldsymbol{p}_0 - \boldsymbol{p}_{\text{ant}}\right\|_2 + \left\|\boldsymbol{p}_{\text{dif}} - \boldsymbol{p}_{\text{far}}\right\|_2 - \left\|\boldsymbol{p}_0 - \boldsymbol{p}_{\text{far}}\right\|_2. \tag{10}$$

In our model, we consider the multiple-KED model with $N = 8$, representing diffracted fields due to: 1) the right and left sides of the user's torso, 2) the top of the user's head, 3) the bottom of the user's torso, 4) right and left sides of the user's head, and 5) two inner sides of the user's legs. Each diffracted path in our model has its applicable angle range. The path from the head top is considered for user-shadowing angles fulfilling $-W_{\text{h}}/2 \le p_x \le W_{\text{h}}/2$. While the path from the head left is applied for user-shadowing angles with $H_{\text{l}} + H_{\text{t}} \le p_z \le H_{\text{l}} + H_{\text{t}} + H_{\text{h}}$. By using (8), our analytical model of the operator $\hat{F}_{\text{body}}(\boldsymbol{\Omega}_{\text{shadow}})$ can be finally written as

$$\hat{F}_{\text{body}}(\boldsymbol{\Omega}_{\text{shadow}}) = \lim_{d_0 \to \infty} \tilde{F}_{\text{body}}(\boldsymbol{\Omega}_{\text{shadow}}, d_0) = \left|\sum_{i=1}^{N} C_{\text{Diff},i} \exp\left(-\text{j}2\pi \frac{\Delta d_i}{\lambda_0}\right)\right|^2 \tag{11}$$

where $|\cdot|$ is an operator to obtain the absolute value; $\Delta d_i = \boldsymbol{s} \cdot (\boldsymbol{p}_{i,\text{dif}} - \boldsymbol{p}_{i,0}) + \|\boldsymbol{p}_{i,\text{dif}} - \boldsymbol{p}_{\text{ant}}\|_2 - \|\boldsymbol{p}_{i,0} - \boldsymbol{p}_{\text{ant}}\|_2$ is the extra propagation distance when $d_0 \to \infty$ in (10); and $\boldsymbol{s}$ is the unit vector of the user-shadowing angle $\boldsymbol{\Omega}_{\text{shadow}}$. It is worth noticing in (11) that the shadowing losses are independent of the antenna's gains.

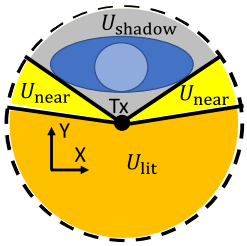


Fig. 3. Lit, shadowed, and near-shadowed regions for the mathematical operators defined from the top view of a human body.

### E. Near-Shadowed Region

We define a set $\mathcal{U} = \{\boldsymbol{\Omega} | \theta \in [0°, 180°], \phi \in [0°, 360°)\}$ to represent angles over a sphere. Fig. 3 defines three angular regions, that is, lit region $\mathcal{U}_{\text{lit}}$, shadowed region $\mathcal{U}_{\text{shadow}}$, and near-shadowed region $\mathcal{U}_{\text{near}}$. The union $\mathcal{U}_{\text{near}} \cup \mathcal{U}_{\text{lit}}$ represents the optical lit region. Since the near-shadowed region $\mathcal{U}_{\text{near}}$ still sees prominent diffractions, and the reflections from the body are negligible compared with the LOS field, we still use the operator of the shadowed region (11) to estimate the body effects even though it is an optical lit region. Therefore, for the *mathematical operators*, we assume $\boldsymbol{\Omega}_{\text{shadow}} \in \mathcal{U}_{\text{near}} \cup \mathcal{U}_{\text{shadow}}$ and $\boldsymbol{\Omega}_{\text{lit}} \in \mathcal{U}_{\text{lit}}$. The boundary between $\mathcal{U}_{\text{near}}$ and $\mathcal{U}_{\text{lit}}$ fulfills the condition that both powers of reflection and diffraction fields are similar and 10 dB weaker than the LOS field.

### F. Spherical Coverage

The spherical coverage, which is an empirical statistic of the maximum gains for each angle over a sphere [19], [21], is evaluated to compare the radiation patterns from full-wave simulations and those derived from our mathematical operator. The former is the ground truth while the latter is a computationally lighter alternative. The comparison shows whether the proposed operator successfully reproduces the antenna array's coverage performance reasonably as compared to the full-wave simulations. Pattern syntheses of a cellphone antenna array are based on equal gain combining for each polarization. CDF plots of spherical coverage are calculated to make the comparison [19], [21]. When deriving the spherical coverage statistics, 10 000 solid angles are spaced uniformly over a sphere.

## III. Testing the Mathematical Operators

In this section, numerical human models for full-wave simulations are introduced, which are employed as the ground truth to make a comparison with our proposed mathematical operators. Then, the hand models with a linear antenna array on the cellphone chassis are introduced, which serve to derive the inputs for the operators. Finally, the performance of the operators is evaluated by comparing their outputs with full-wave simulations.

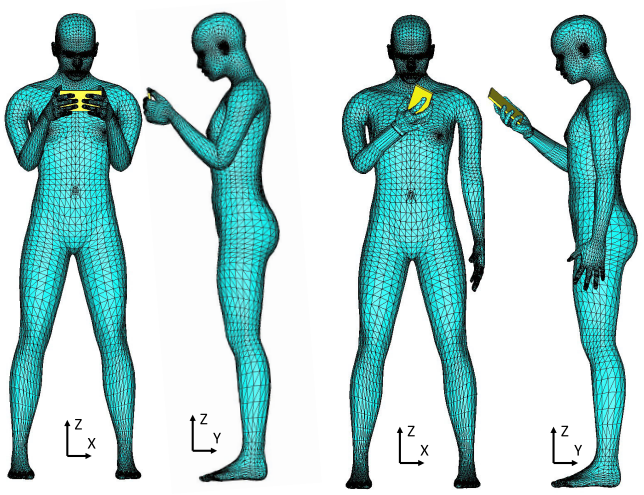


(a) (b)

Fig. 4. Front view and the side view of a human model made by *Makehuman* software for (a) landscape mode and (b) portrait mode; the yellow box is a cellphone chassis.

### A. Numerical Human Models

Our proposed operators, that is, (7) and (11) for the lit and shadowed regions, are tested by two kinds of user modes, namely landscape and portrait modes, at 28-GHz radio frequency. Their numerical models are generated by open-source software, that is, *Makehuman*, as shown in Fig. 4. The permittivity of human skin, $\epsilon_r = 16.55$ and $\sigma = 25.82$ S/m [21], is used to model the whole body of humans [19], [21] due to the shallow skin depth at 28 GHz. Although the skin permittivity is not homogeneous for a real person, its influence on the radiation patterns is negligible [33]. Therefore, the skin is modeled by homogeneous impedance boundaries in full-wave simulations. The full-wave simulation is implemented in *CST Studio Suite*, and the relevant setup is detailed in [18], which was verified against measurements [19].

### B. Inputs for the Proposed Operators

For the lit region, $\boldsymbol{E}_0$ needs to be derived as the inputs for (7), so the radiation patterns with hand effects were obtained by full-wave simulations at 28 GHz. The two-hand model and one-hand model with cellphone chassis, composing Fig. 4, are shown in Figs. 5(a) and 6(a). The antenna–hand interaction simulation is detailed [21], including experimental verification. Two four-element dual-polarized linear patch antenna arrays on the cellphone-sized copper box are excited by discrete ports as illustrated in Figs. 5(b) and 6(b). The radiation patterns of selected ports of the two antenna arrays are, respectively, shown in Fig. 7. There are some ripples in the radiation patterns due to reflections from palms for the two-hand model in the landscape mode, while finger-shadowing effects appear in the plots for the one-hand model in the portrait mode.

### C. Mathematical Operators Applied to Cellphone Modes

When using the mathematical operators, the same human skin's permittivity at 28 GHz, $\epsilon_r = 16.55$ and $\sigma = 25.82$ S/m,

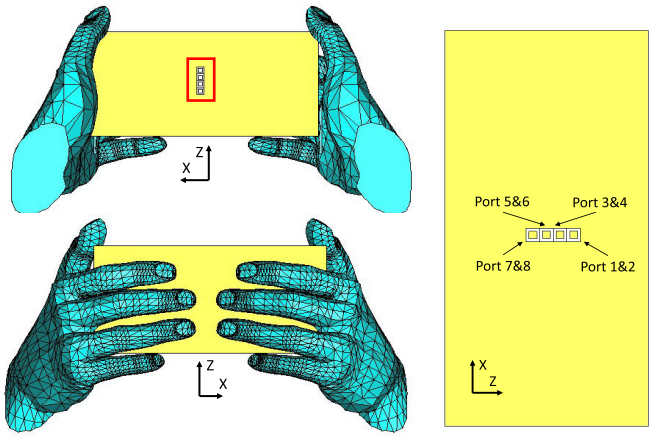


(a) (b)

Fig. 5. (a) Top and bottom views of the two-hand numerical model with a cellphone chassis. (b) Antenna configuration of the cellphone chassis ($75 \times 150 \times 8$ mm$^3$) for the two-hand simulation.

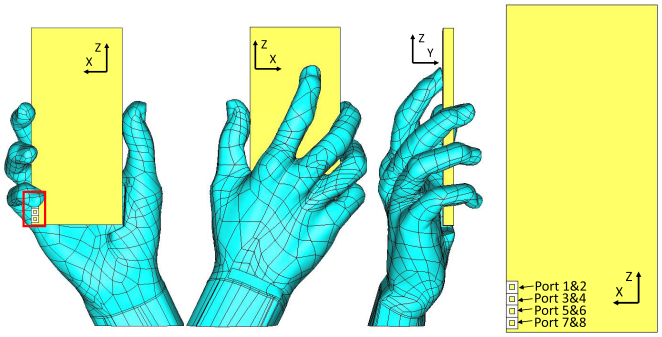


(a) (b)

Fig. 6. (a) Top, bottom, and side views of the one-hand numerical model with a cellphone chassis. (b) Antenna configuration of the cellphone chassis ($75 \times 150 \times 8$ mm$^3$) for the one-hand simulation.

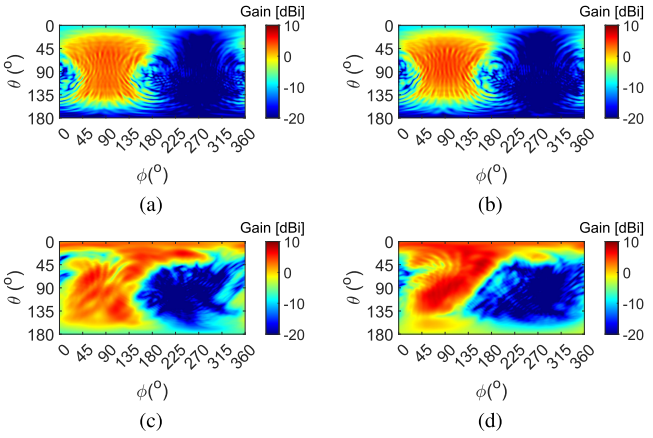


Fig. 7. Radiation pattern of the antenna array with hand effects ($G_{\text{hand,full}}(\boldsymbol{\Omega})$) for landscape mode's (a) Port 3 and (b) Port 7 and for portrait mode's (c) Port 3 and (d) Port 7.

is used as the full-wave simulations. The same dimensions of the human body are considered for the full-wave simulations and operators as found in Table I. In the following plots, the step of angles along both $\theta$ and $\phi$ is 1°.

*1) Cellphone in the Landscape Mode:* The spacing $d_y$ between cellphone antennas and the user body along the $y$-axis

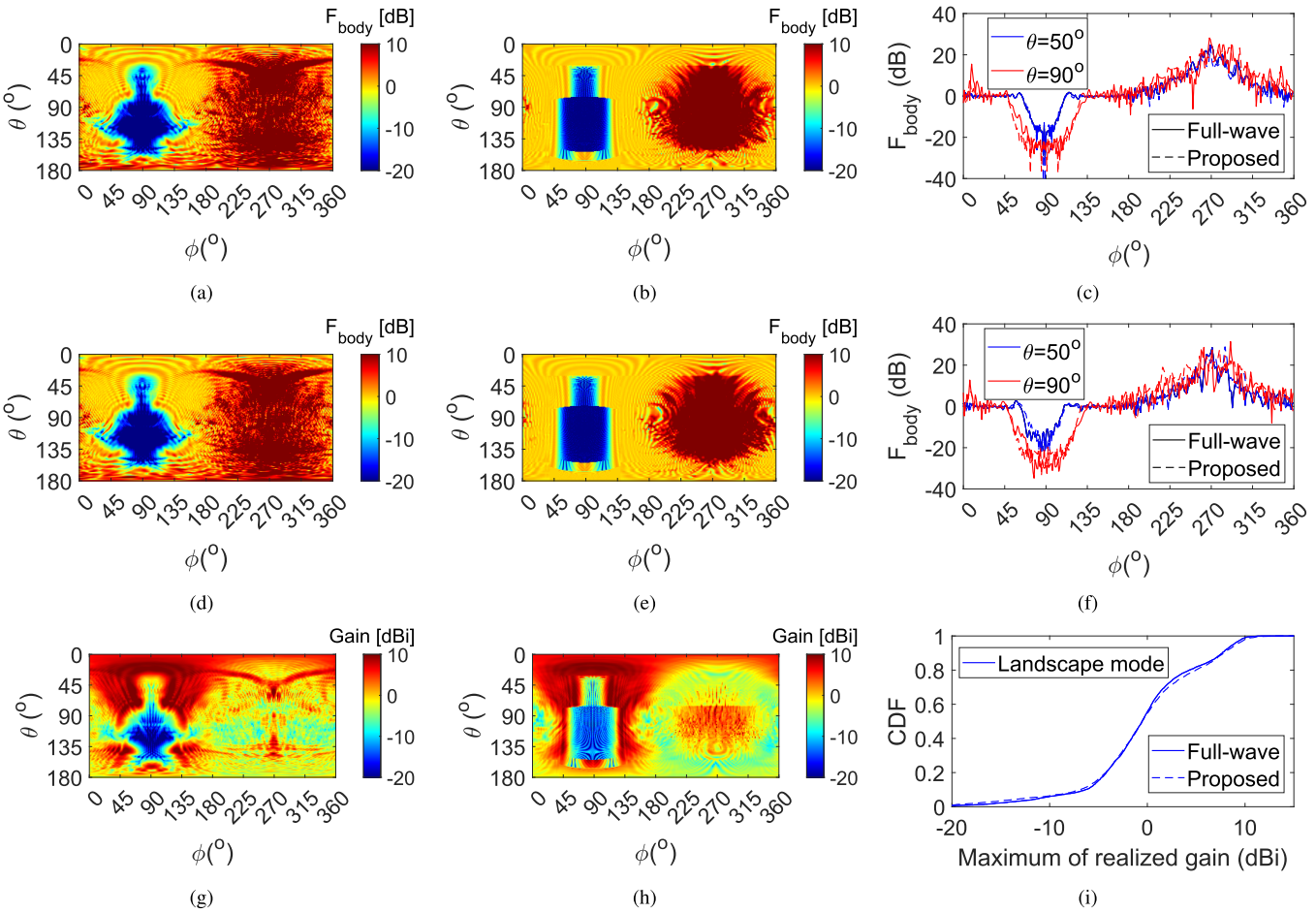


Fig. 8. $F_{\text{body}}(\boldsymbol{\Omega})$ of the Port 3 antenna defined in Fig. 5 for (a) complex human model in Fig. 4(a) with full-wave simulation and (b) proposed operator. (c) Azimuth plots of (a) and (b). $F_{\text{body}}(\boldsymbol{\Omega})$ of the Port 7 antenna defined in Fig. 5 for (d) complex human model in Fig. 4(a) with full-wave simulation and (e) proposed operator. (f) Azimuth plots of (d) and (e). Spherical coverage of (g) complex human model and (h) proposed operator. (i) CDF plots of the spherical coverage.

is 35.0 cm. The Array's center location $\boldsymbol{O} = (0, 0, 0)$ cm is 10.0 cm below the shoulder top along the $z$-axis. For the proposed operator, we define $\boldsymbol{\Omega}_{\text{shadow}} \in \{\boldsymbol{\Omega} | \theta \in [32°, 180°], \phi \in [40°, 140°]\}$ and the rest is the lit region $\boldsymbol{\Omega}_{\text{lit}}$ in the spherical coordinate system.

We can obtain $F_{\text{body,full}}(\boldsymbol{\Omega}) = (G_{\text{body,full}}(\boldsymbol{\Omega}))/(G_{\text{hand,full}}(\boldsymbol{\Omega}))$ by full-wave simulations. Their comparison with the operators $\hat{F}_{\text{body}}(\boldsymbol{\Omega})$ is shown in Fig. 8. We choose Ports 3 and 7 shown in Fig. 8(a) and (d) as examples since all the ports' field distributions are very similar to each other. The operator reproduces the full-wave simulations with the complex human model to a large extent. The hemisphere defined in Fig. 1 reproduces the field fluctuations above the user's head [Fig. 8(a) and (d)] as shown in Fig. 8(b) and (c). Still, discontinuities can be seen in Fig. 8(b) and (c) since the human model assumed in the operator is a combination of planar, cylindrical, and spherical structures, each of which has its working angle range when using KED and GO. Compared with full-wave simulations, the shadowing angular width and losses are similar for two cuts at $\theta = 50°$ and 90°, which can be seen in Fig. 8(c). When it comes to the lit region, the reflected power levels are predicted with a less than 2-dB difference at $\phi$ close to 270° on average. A similar trend can be found in Fig. 8(f). The spherical coverage of the whole antenna array is calculated as shown in Fig. 8(g) and (h) by using (1) for the full-wave simulations and the proposed operator, respectively. We can find that the proposed operator has higher reflections in $\theta \in [90°, 135°]$ than the full-wave simulations. This is because the operator assumes a simplified human body that has smooth curvatures, which bring about slightly higher reflection coefficients. The cdf curves in Fig. 8(i) show that their statistical characteristics have a close agreement. The difference is 0.8 dB at cdf = 0.8 level and up to 1.4 dB at cdf = 0.05 corresponding to the shadowed region.

*2) Cellphone in the Portrait Mode:* To further verify the proposed operator, another user mode of portrait cellphone posture is studied. The dimensions of the user body are the same as landscape mode, shown in Table I. In addition, $d_y = 30$ cm along the $y$-axis, and the array's central location $(70, 0, 0)$ cm is 15.0 cm below the shoulder top along the $z$-axis. It is worth noticing that Ports 1–4 of the dual-polarized antenna array were shadowed by a finger in the normal direction of the antenna as shown in Fig. 6(a). For the proposed operator, we define $\boldsymbol{\Omega}_{\text{shadow}} \in \{\boldsymbol{\Omega} | \theta \in [21°, 180°], \phi \in [40°, 150°]\}$ and the rest belongs to $\boldsymbol{\Omega}_{\text{lit}}$.

The full-wave simulations and the proposed operator are compared in Fig. 9. We only choose Ports 3 and 7 to show user effects in Fig. 9(a) and (d) since all the ports' field distributions

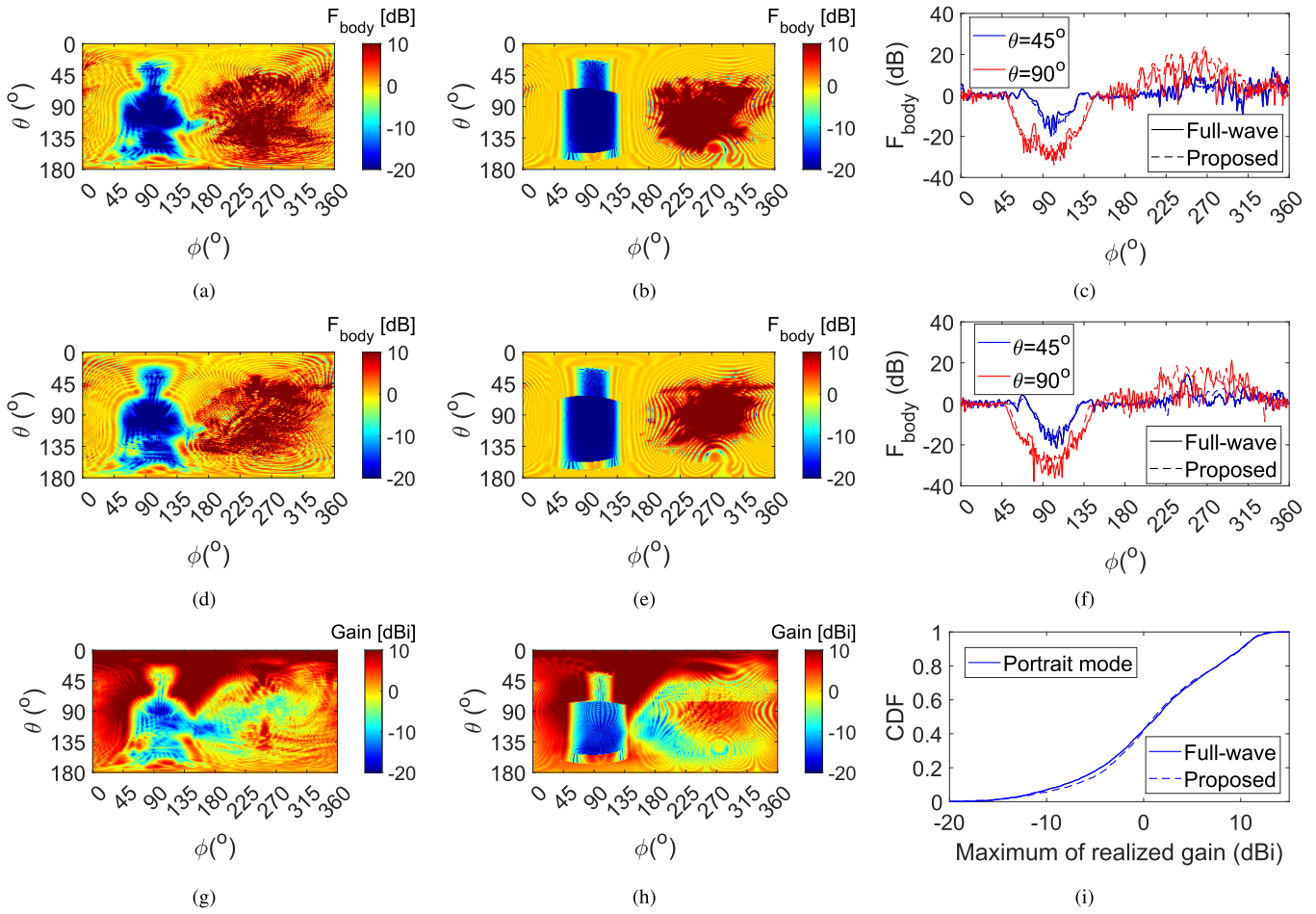


Fig. 9. $F_{\text{body}}(\boldsymbol{\Omega})$ of the Port 3 antenna defined in Fig. 6 for (a) complex human model in Fig. 4(b) with full-wave simulation and (b) proposed operator. (c) Azimuth plots of (a) and (b). $F_{\text{body}}(\boldsymbol{\Omega})$ of the Port 7 antenna defined in Fig. 6 for (d) complex human model in Fig. 4(b) with full-wave simulation and (e) proposed operator. (f) Azimuth plots of (d) and (e). Spherical coverage of (g) complex human model and (h) proposed operator. (i) CDF plots of the spherical coverage.

are very similar to each other. Similar to the landscape mode, the proposed operator reproduces the full-wave simulations to a large extent, and similar discontinuities can also be seen. The pattern cuts in Fig. 9(c) show about 3.2 dB (4.5 dB) difference in the lit region at angles, $\theta = 45°(90°)$ and $\phi$ close to 270° on average, while the difference in the shadowed region is smaller. The differences are attributed to constructive and destructive interference of reflected waves from various parts of the body. The fluctuation is a stochastic process similar to small-scale channel fading of received signal strength in mobile channels. A similar trend can be found in Fig. 9(f). The statistical characteristics of antenna patterns, that is, the spherical coverage, are, therefore, more important in practical link evaluation [19]. The spherical coverage of the whole antenna array is calculated for the full-wave simulations and the proposed operator as shown in Fig. 9(g) and (h). We can find that the proposed operator has higher reflections in $\theta \in [90°, 135°]$ than the full-wave simulations, similar to the landscape mode. However, the cdf curves show that their statistical characteristic has a close agreement. The major difference is around 1.0 dB at cdf = 0.2 level, corresponding to the green color region in Fig. 9(h).

*3) Other Cases:* After testing the two vital user modes, we also applied our proposed operator to more cases as follows.

1) We set $d_y = 50.0$ cm and $d_y = 20.0$ cm for the landscape mode.
2) We changed the orientation of the cellphone chassis by ±20° along $\theta$ for the landscape mode.
3) We put cellphone antennas in front of a human without hand holding, emulating the case that the user holds a selfie stick for cellphones.
4) We changed the operating frequency to 39 GHz for the landscape mode.
5) We applied the operator to a different size of the human model for the landscape mode. The obtained spherical coverage cdf shows a difference of less than 1.2 dB for all these cases. Because of brevity, those results are not shown here.

*4) Applicability of the Mathematical Operator:* The proposed operator primarily models scenarios where a user stands and uses a cellphone operating at 5G mmW frequencies. In Section III-C, we conducted tests in various conditions and found that the operator can adapt to different antenna

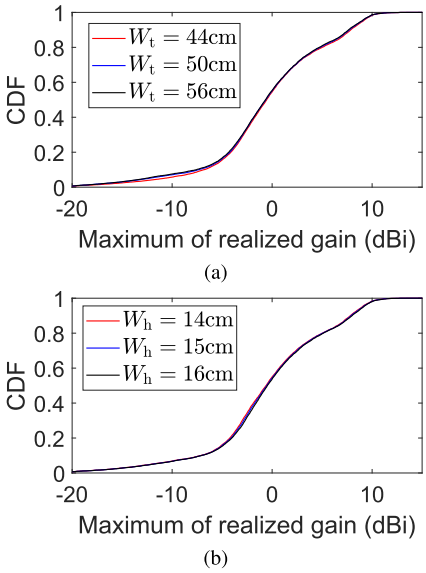


Fig. 10. (a) CDF of spherical coverage for different torso widths ($W_t$). (b) CDF of spherical coverage for different head widths ($W_h$).

positions and orientations. Even at higher 5G mmW frequencies, it maintains good accuracy for statistical characteristics, indicating robustness in scenarios involving a standing user using a cellphone.

However, for other human postures such as sitting, running, or answering a phone call, the operator requires modification and further testing in future studies. Regarding frequency dependency, the shadowing part can be extended to different frequencies because the knife-edge model includes frequency-based diffraction and has been used in many papers for human-blockage modeling [2], [5], [9], [13], [29], [35]. Nevertheless, the backscattering part of the model exhibits frequency dependency, considering it includes only the first bounce of reflection and the high-frequency assumption nature of GO. As discussed in Section II-C, high-order reflections at 5G mmWs are usually negligible due to human skin properties. However, when these reflections become significant, the operator's accuracy decreases. Additionally, the operator assumes that the user is within the Fresnel region of the cellphone antenna array; it may not be effective if the user is within the reactive near-field region.

*5) Impacts of Human Body Dimensions:* To assess the impact of input human dimensions on the statistical characteristics of human-affected antenna patterns, we employ the landscape mode model to calculate the cdf of spherical coverage. We keep the input human sizes unchanged, as shown in Table I, except for the torso width ($W_t$) and head width ($W_h$). Then, we can obtain the cdf curves depicted in Fig. 10. It can be seen that the maximum difference 0.3 dB happens at cdf = 0.3 level when $W_h$ is from 14 to 16 cm. In addition, $W_t$ mainly influences the cdf ≈0.1 and ≈0.8 levels. When it changes from 46 to 54 cm, the major difference is around 1.7 dB at cdf = 0.07. Hence, we conclude that a roughly realistic representation of human dimensions suffices when our emphasis lies solely on the statistical characteristics of human effects on 5G mmW mobile antennas.

TABLE II
COMPARISONS BETWEEN THE PROPOSED MODEL AND FULL-WAVE SIMULATIONS

| | Proposed model | Full-wave simulations |
|---|---|---|
| Input information | 1) Antenna patterns<br>2) User dimensions<br>3) phone orientation | 1) Antenna patterns<br>2) Three-dimensional human model |
| Time duration to solve radiation [ min.] | 1) Calculation of inputs [380]<br>2) Derivation of body effects [0.6] | 1) Calculation of inputs [380]<br>2) Derivation of body effects [2100] |

### D. Comparisons of Computational Load

Table II compares a computational load for full-wave simulations and our proposed operators at 28 GHz. The operating computer's CPU is *Intel* Xeon[2] E3-1230 and the RAM is 16 GB. The inputs are antenna radiation patterns with hand effects for our testing cases, which were derived from full-wave simulations. Calculation of the inputs took 380 min on our operating computer. The table shows that the proposed operator can save much time when reproducing body effects on antenna radiations.

## IV. CONCLUSION

This manuscript proposes an approach to model user body effects on radiations of cellphone antennas in the 5G mmW band. By implementing full-wave simulations, the antenna gains with hand effects are obtained as inputs for our proposed operators, consisting of KED and GO. Comparisons between the proposed operator and the full-wave simulations with referential complex human models show a good agreement for the statistical characteristic of spherical coverage and cuts of radiation patterns, meaning that the statistical characteristic of the 5G mmW radio channels for the user body effects is modeled properly. They indicate the following.

1) KED model, defined in the Fraunhofer region, applies to the Fresnel region of radiated fields from mobile antennas in typical use cases.
2) GO can reproduce the statistical characteristic of the antenna array's radiations to a large extent.
3) The proposed model has a clear advantage in deriving user effects on mmW cellphone communications. It can be used in simulations of indoor and outdoor mmW cellphone communication channels. Even when lacking practical human models, the proposed operator allows us to predict the antenna array's statistical characteristics within a reduced time.

## APPENDIX

Here, the mathematical and physical principles for reflection rays on arbitrary curvatures are summarized.

Spherical-wave reflection on a curvature is described in Fig. 11. For an incident spherical wavefront, $\rho_{r,1}$ and $\rho_{r,2}$ can be obtained by

$$\frac{1}{\rho_{r,1}} = \frac{1}{s_i} + \frac{1}{f_1} \tag{12}$$

[2]Registered trademark.

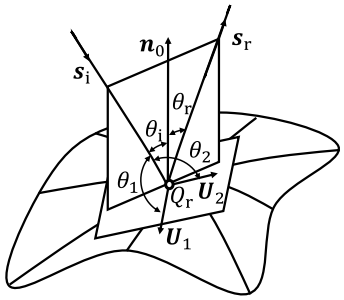


Fig. 11. Schematic of the spherical-wave reflection at a curvature.

and

$$\frac{1}{\rho_{r,2}} = \frac{1}{s_i} + \frac{1}{f_2} \tag{13}$$

where $s_i$ is the travel distance of the incident wave from the source to the reflection point $Q_r$; $f_{1,2}$ can be written as

$$f_{1,2} = \frac{1}{\cos\theta_i}\left[\frac{\sin^2\theta_2}{a_1} + \frac{\sin^2\theta_1}{a_2}\right] \pm \sqrt{\frac{1}{\cos^2\theta_i}\left[\frac{\sin^2\theta_2}{a_1} + \frac{\sin^2\theta_1}{a_2}\right]^2 - \frac{4}{a_1 a_2}} \tag{14}$$

where the plus sign corresponds to $f_1$ and the minus sign to $f_2$; $\theta_1 = \cos^{-1}(-\boldsymbol{s}_i \cdot \boldsymbol{U}_1)$ and $\theta_2 = \cos^{-1}(-\boldsymbol{s}_i \cdot \boldsymbol{U}_2)$, where $\boldsymbol{s}_i$ is the unit vector of incident direction; $\boldsymbol{U}_1$ and $\boldsymbol{U}_2$ are the orthogonal unit vector on the reflection plane and $\boldsymbol{U}_i \cdot \boldsymbol{n}_0 = 0$, $i = 1, 2$; $\boldsymbol{n}_0$ is the normal vector of the curvature at $Q_r$; $a_1$ and $a_2$ are the curvature radii at $Q_r$. For an elliptic cylinder for backscattering field calculation due to a body, the coordinate of any points on the surface can be represented by $[a\cos\phi, b\sin\phi, z]$. Therefore, $a_1 = +\infty$ and $a_2 = a^2b^2((\cos^2\phi/a^2) + (\sin^2\phi/b^2))^{(3/2)}$, where $\phi$ is the polar coordinate and the elliptic center is the coordinate origin; $a$ is the radius along the $x$-axis, while $b$ is the radius along the $y$-axis. For an ellipsoid, the coordinate of any points on the surface can be represented by $[a\cos\phi\cos\theta, a\sin\phi\cos\theta, b\cos\theta]$. Therefore, $a_1 = a\sin\theta$ and $a_2 = a^2b^2((\sin^2\theta/a^2) + (\cos^2\theta/b^2))^{(3/2)}$.

## REFERENCES


[1] M. Ghaddar, L. Talbi, T. A. Denidni, and A. Sebak, "A conducting cylinder for modeling human body presence in indoor propagation channel," *IEEE Trans. Antennas Propag.*, vol. 55, no. 11, pp. 3099–3103, Nov. 2007.

[2] J. Kunisch and J. Pamp, "Ultra-wideband double vertical knife-edge model for obstruction of a ray by a person," in *Proc. IEEE Int. Conf. Ultra-Wideband*, Hannover, Germany, vol. 2, Sep. 2008, pp. 17–20.

[3] C. Gustafson and F. Tufvesson, "Characterization of 60 GHz shadowing by human bodies and simple phantoms," in *Proc. 6th Eur. Conf. Antennas Propag. (EUCAP)*, Mar. 2012, pp. 473–477.

[4] M. Jacob, S. Priebe, R. Dickhoff, T. Kleine-Ostmann, T. Schrader, and T. Kurner, "Diffraction in mm and sub-mm wave indoor propagation channels," *IEEE Trans. Microw. Theory Techn.*, vol. 60, no. 3, pp. 833–844, Mar. 2012.

[5] M. Jacob et al., "Extension and validation of the IEEE 802.11ad 60 GHz human blockage model," in *Proc. 7th Eur. Conf. Antennas Propag. (EuCAP)*, Apr. 2013, pp. 2806–2810.

[6] N. Tran, T. Imai, and Y. Okumura, "Study on characteristics of human body shadowing in high frequency bands: Radio wave propagation technology for future radio access and mobile optical networks," in *Proc. IEEE 80th Veh. Technol. Conf. (VTC-Fall)*, Sep. 2014, pp. 1–5.

[7] M. Nakamura, M. Sasaki, N. Kita, and Y. Takatori, "Path loss model in crowded areas considering multiple human blockage at 4.7 and 26.4 GHz," in *Proc. IEEE Conf. Antenna Meas. Appl. (CAMA)*, Dec. 2017, pp. 40–43.

[8] J. S. Romero-Peña and N. Cardona, "Applicability limits of simplified human blockage models at 5G mm-wave frequencies," in *Proc. 13th Eur. Conf. Antennas Propag. (EuCAP)*, Mar. 2019, pp. 1–5.

[9] U. T. Virk and K. Haneda, "Modeling human blockage at 5G millimeter-wave frequencies," *IEEE Trans. Antennas Propag.*, vol. 68, no. 3, pp. 2256–2266, Mar. 2020.

[10] D. Prado-Alvarez, S. Inca, D. Martín-Sacristán, and J. F. Monserrat, "Millimeter-wave human blockage model enhancements for directional antennas and multiple blockers," *IEEE Commun. Lett.*, vol. 25, no. 9, pp. 2776–2780, Sep. 2021.

[11] A. Singh, G. Ghatak, A. Srivastava, V. A. Bohara, and A. K. Jagadeesan, "Performance analysis of indoor communication system using off-the-shelf LEDs with human blockages," *IEEE Open J. Commun. Soc.*, vol. 2, pp. 187–198, 2021.

[12] A. Shafie, N. Yang, S. Durrani, X. Zhou, C. Han, and M. Juntti, "Coverage analysis for 3D terahertz communication systems," *IEEE J. Sel. Areas Commun.*, vol. 39, no. 6, pp. 1817–1832, Jun. 2021.

[13] X. Chen, L. Tian, P. Tang, and J. Zhang, "Modelling of human body shadowing based on 28 GHz indoor measurement results," in *Proc. IEEE 84th Veh. Technol. Conf. (VTC-Fall)*, Sep. 2016, pp. 1–5.

[14] C. Slezak, V. Semkin, S. Andreev, Y. Koucheryavy, and S. Rangan, "Empirical effects of dynamic human-body blockage in 60 GHz communications," *IEEE Commun. Mag.*, vol. 56, no. 12, pp. 60–66, Dec. 2018.

[15] K. Yoshikawa and T. Hayashi, "Experimental study of loss and variation of human blockage for terahertz wireless communications," in *Proc. 16th Eur. Conf. Antennas Propag. (EuCAP)*, Mar. 2022, pp. 1–5.

[16] C. Slezak and S. Rangan, "Measurement-based indoor millimeter wave blockage models," *IEEE Trans. Wireless Commun.*, vol. 21, no. 8, pp. 6774–6786, Aug. 2022.

[17] V. Raghavan et al., "Spatio-temporal impact of hand and body blockage for millimeter-wave user equipment design at 28 GHz," *IEEE Commun. Mag.*, vol. 56, no. 12, pp. 46–52, Dec. 2018.

[18] M. Heino, C. Icheln, and K. Haneda, "Self-user shadowing effects of millimeter-wave mobile phone antennas in a browsing mode," in *Proc. 13th Eur. Conf. Antennas Propag. (EuCAP)*, Mar. 2019, pp. 1–5.

[19] L. Vähä-Savo et al., "Empirical evaluation of a 28 GHz antenna array on a 5G mobile phone using a body phantom," *IEEE Trans. Antennas Propag.*, vol. 69, no. 11, pp. 7476–7485, Nov. 2021.

[20] C. Ballesteros, L. Vähä-Savo, K. Haneda, C. Icheln, J. Romeu, and L. Jofre, "Assessment of mmWave handset arrays in the presence of the user body," *IEEE Antennas Wireless Propag. Lett.*, vol. 20, no. 9, pp. 1736–1740, Sep. 2021.

[21] B. Xue, P. Koivumäki, L. Vähä-Savo, K. Haneda, and C. Icheln, "Impacts of real hands on 5G millimeter-wave cellphone antennas: Measurements and electromagnetic models," *IEEE Trans. Instrum. Meas.*, vol. 72, pp. 1–12, 2023.

[22] I. Syrytsin, S. Zhang, G. F. Pedersen, K. Zhao, T. Bolin, and Z. Ying, "Statistical investigation of the user effects on mobile terminal antennas for 5G applications," *IEEE Trans. Antennas Propag.*, vol. 65, no. 12, pp. 6596–6605, Dec. 2017.

[23] I. Syrytsin, S. Zhang, and G. F. Pedersen, "User impact on phased and switch diversity arrays in 5G mobile terminals," *IEEE Access*, vol. 6, pp. 1616–1623, 2018.

[24] K. Zhao, J. Helander, D. Sjöberg, S. He, T. Bolin, and Z. Ying, "User body effect on phased array in user equipment for the 5G mmWave communication system," *IEEE Antennas Wireless Propag. Lett.*, vol. 16, pp. 864–867, 2017.

[25] K. Zhao, Z. Ying, S. Zhang, and G. Pedersen, "User body effects on mobile antennas and wireless systems of 5G communication," in *Proc. 14th Eur. Conf. Antennas Propag. (EuCAP)*, Mar. 2020, pp. 1–5.

[26] *5G: Study on channel model for frequencies from 0.5 to 100 GHz*, ETSI document TR 138 901, Version 16.1.0, Release 16, 3GPP, Nov. 2020. [Online]. Available: https://www.etsi.org/deliver/etsi_tr/138900_138999/138901/16.01.00_60/tr_138901v160100p.pdf

[27] L. Vähä-Savo, P. Koivumäki, K. Haneda, C. Icheln, and J. Chen, "3-D modeling of human hands for characterizing antenna radiation from a 5G mobile phone," in *Proc. 16th Eur. Conf. Antennas Propag. (EuCAP)*, Mar. 2022, pp. 1–5.

[28] A. V. Osipov and S. A. Tretyakov, *Modern Electromagnetic Scattering Theory With Applications*. Hoboken, NJ, USA: Wiley, 2017.

[29] D. A. McNamara, C. W. Pistorius, and J. Malherbe, *Introduction to the Uniform Geometrical Theory of Diffraction*. Norwood, MA, USA: Artech House, 1990.

[30] W. D. Burnside, "Computer modeling of electromagnetic problems using the geometrical theory of diffraction," in *Proc. IEEE Int. Symp. Electromagn. Compat.*, Jul. 1976, pp. 1–5.

[31] R. Brem and T. F. Eibert, "A shooting and bouncing ray (SBR) modeling framework involving dielectrics and perfect conductors," *IEEE Trans. Antennas Propag.*, vol. 63, no. 8, pp. 3599–3609, Aug. 2015.

[32] D. M. Pozar, *Microwave Engineering*. Hoboken, NJ, USA: Wiley, 2011.

[33] S. S. Zhekov, O. Franek, and G. F. Pedersen, "Dielectric properties of human hand tissue for handheld devices testing," *IEEE Access*, vol. 7, pp. 61949–61959, 2019.

[34] R. Luebbers, "Finite conductivity uniform GTD versus knife edge diffraction in prediction of propagation path loss," *IEEE Trans. Antennas Propag.*, vol. AP-32, no. 1, pp. 70–76, Jan. 1984.

[35] M. Jacob, S. Priebe, A. Maltsev, A. Lomayev, V. Erceg, and T. Kürner, "A ray tracing based stochastic human blockage model for the IEEE 802.11ad 60 GHz channel model," in *Proc. 5th Eur. Conf. Antennas Propag. (EUCAP)*, Apr. 2011, pp. 3084–3088.

**Bing Xue** (Graduate Student Member, IEEE) was born in Henan, China. He is currently pursuing the D.Sc. (Tech.) degree in radio engineering with the School of Electrical Engineering, Aalto University, Espoo, Finland.

His current research interests include antenna designs and measurements, human–antenna interaction simulation and measurements, and electromagnetic modeling focusing on mm-wave frequencies for 5G systems and beyond.

**Katsuyuki Haneda** (Member, IEEE) is an Associate Professor with the School of Electrical Engineering, Aalto University, Espoo, Finland. His current research activity covers high-frequency radios such as millimeter-waves and beyond and wireless for medical and smart-city applications.

Dr. Haneda was the author and coauthor of several best paper and student paper awards at the IEEE Vehicular Technology Conference and European Conference on Antennas and Propagation, among others. He received the R. W. P. King Paper Award from IEEE TRANSACTIONS ON ANTENNAS AND PROPAGATION in 2021, together with Dr. Usman Virk. He was the Technical Program Committee Co-Chair of the 17th European Conference on Antennas and Propagation (EuCAP 2023), Florence, Italy. He was an Associate Editor of IEEE TRANSACTIONS ON ANTENNAS AND PROPAGATION from 2012 to 2016 and an Editor of IEEE TRANSACTIONS ON WIRELESS COMMUNICATIONS from 2013 to 2018. He was the Guest Editor of Special Issues on IEEE Antennas and Propagation Aspects of In-Band Full-Duplex Applications and IEEE Artificial Intelligence in Radio Propagation for Communications from IEEE TRANSACTIONS ON ANTENNAS AND PROPAGATION in 2021 and 2022, respectively.

**Pasi Koivumäki** (Member, IEEE) received the M.Sc. (Tech.) degree (Hons.) from the School of Electrical Engineering, Aalto University, Espoo, Finland, in 2017, where he is currently pursuing the D.Sc. (Tech.) in radio engineering.

His current research activities include multiband radio channel measurements, simulations, and modeling focusing on mm-wave frequencies for 5G systems and beyond. His particular interests lie in ray-launching and ray-tracing algorithms for propagation and channel modeling in urban environments of future smart cities and their combined effects on cellular coverage and quality of service.

**Clemens Icheln** received the Dipl.-Ing. degree in electrical engineering from the Harburg University of Technology, Hamburg, Germany, in 1996, and the Licentiate and D.Sc. Tech. degrees in radio engineering from Aalto University, Espoo, Finland, in 1999 and 2001, respectively.

He is currently a University Lecturer with the Department of Electronics and Nanoengineering, School of Electrical Engineering, Aalto University. His current research interests include the design of multielement antennas for small communication devices such as mobile terminals and medical implants, to operate at frequency ranges as low as 400 MHz but also up to mm-wave frequencies, as well as the development of suitable antenna characterization methods that allow taking, for example, the effects of the radio channel into account.